ROYAL SOCIETY OF CHEMISTRY

## PAPER

Check for updates

# Understanding the structural and charge transport property relationships for a variety of merocyanine single-crystals: a bottom up computational investigation†

Nora Gildemeister,[a] Gaetano Ricci,‡[b] Lukas Böhner,[a] Jörg M. Neudörfl,[c] Dirk Hertel,[a] Frank Würthner, [id][de] Fabrizia Negri, [id] *[bf] Klaus Meerholz*[a] and Daniele Fazzi [id] *[a]

Merocyanines consist of electronic donor (D) and acceptor (A) subunits connected *via* a methine bridge. They are highly polar organic π-conjugated molecules investigated for their self-assembly and optoelectronic properties. The accurate description of their structure–property relationships remains challenging. We report a comprehensive analysis modelling intra- and inter-molecular charge transport parameters for a library of merocyanines featuring different D/A combinations and lateral substituents. We found that constrained DFT correctly assesses the molecular and electronic structure in single crystals. The most effective charge transport pathways were identified and charge carrier mobilities were computed. We analyzed a large variety of single crystals highlighting the impact of alkyl substituents and casting conditions, drawing clear structure *vs.* charge transport relationships. Our modelling suggests that hole transport is maximized when dipolar molecules are packed in slipped not centrosymmetric pairs, arranged in 2D interconnected architectures. Computed and experimental charge mobilities for single crystals are in good agreement.

## 1. Introduction

A remarkable aspect of π-conjugated molecular materials is the possibility to tune their properties (*e.g.*, electrical, optical, magnetic) by manipulating their structure, from the single molecule up to the supramolecular level. Prominent examples belong to the class of dipolar π-conjugated molecules, in which the absorption and emission spectra can be altered by changing the donor (D) and acceptor (A) groups, or by inducing structural reorganizations *via* thermal annealing or solvent casting procedures. Amongst D/A conjugated systems,[1] merocyanines are one of the most studied compounds over the past four decades.[2] Their ability to tune the optical gap *via* chemical and physical approaches made them good candidates for opto-electronic applications.

Merocyanines were extensively investigated in various applications, from textile colorants towards more high-tech solutions.[3] Pioneering works by Marder,[4] Blanchard-Desce,[5] Meerholz and Würthner[6,7] paved the way towards their application in the area of nonlinear optics,[1,8] photorefractivity,[6,9,10] solar cells (OSC),[11] and only recently organic field effect transistors (OFETs). Initially, it was believed that merocyanines would be poor p-type semiconductors due to their strong dipolar character.[12,13] However, over the last two decades, researchers were able to increase the charge carrier mobility ($\mu$) of merocyanines by orders of magnitude ($10^{-5}$–2 cm$^2$ V$^{-1}$ s$^{-1}$),[14–16] approaching or even surpassing values as high as those of gold-standard organic semiconductors, like tetracene (2.4 cm$^2$ V$^{-1}$ s$^{-1}$),[17] TIPS-pentacene (5.0 cm$^2$ V$^{-1}$ s$^{-1}$)[18] and copper phthalocyanine (1.0 cm$^2$ V$^{-1}$ s$^{-1}$).[19] Even though merocyanines have not reached the performance of archetype p-type single crystalline molecular semiconductors (*e.g.*, rubrene,

[a] *Institut für Physikalische Chemie, Department für Chemie, Universität zu Köln, Greinstr. 4-6, 50939 Köln, Germany. E-mail: klaus.meerholz@uni-koeln.de, dfazzi@uni-koeln.de*

[b] *Università di Bologna, Dipartimento di Chimica 'Giacomo Ciamician', Via F. Selmi, 2, 40126 Bologna, Italy. E-mail: fabrizia.negri@unibo.it*

[c] *Institut für Organische Chemie, Department für Chemie, Universität zu Köln, Greinstr. 4-6, 50939 Köln, Germany*

[d] *Institut für Organische Chemie, Universität Würzburg, Am Hubland, 97074 Würzburg, Germany*

[e] *Center for Nanosystems Chemistry, Universität Würzburg, Am Hubland, 97074 Würzburg, Germany*

[f] *INSTM UdR Bologna, Via F. Selmi, 2, 40126 Bologna, Italy*

‡ Present address: Unité de Chimie Physique Théorique et Structurale and Laboratoire de Physique du Solide, Namur Institute of Structured Matter, Université de Namur, B-5000 Namur, Belgium.

This journal is © The Royal Society of Chemistry 2021

*J. Mater. Chem. C*, 2021, **9**, 10851–10864 | **10851**

$\mu \sim 40$ cm$^2$ V$^{-1}$ s$^{-1}$)[20] yet, their highly tunable structural and opto-electronic properties make them unique and versatile functional materials.

In this regard, merocyanines represent the prototypical system for understanding the role played by inter-molecular interactions in affecting the supramolecular architecture. By modulating the bulkiness of the side groups or the D/A units, crystals with different molecular packing motifs were obtained, allowing to correlate the structure with respect to, for instance, the exciton and the charge transport properties.[21–25] In particular for the field of vacuum-processable organic solar cells, merocyanines are among the best donor materials because they inherit high absorptivity and in some cases (*vide infra*) good hole mobility at rather small molecular size, as required for sublimation.[26,27]

Liess *et al.* demonstrated that moving from rigid/small to flexible/large side groups for a given π-conjugated merocyanine, the molecular packing varies from card- to slipped-stack arrangements, strongly affecting the optical and charge transfer properties. Card- and slipped-stack aggregates lead to H- and J-exciton couplings, respectively, causing a blue- or red-shift of the absorption band with respect to that of the monomer. Such features were successfully exploited for ultranarrow bandwidth organic photodiodes.[28]

Similarly, a modulation of the hole mobility by orders of magnitude was achieved for poly-crystalline films[28] by controlling the casting conditions, ranging from $2.4 \times 10^{-3}$ cm$^2$ V$^{-1}$ s$^{-1}$ for solution processed thin films up to $4.8–6.0 \times 10^{-1}$ cm$^2$ V$^{-1}$ s$^{-1}$ for vacuum-deposited layers.[16]

Supporting an earlier observation by Brückstürmer *et al.*,[3] it was found that it is not the high permanent dipole moment of merocyanines limiting their charge-carrier (hole) mobility, but rather the way they self-assemble in crystalline domains.[29] Notably, in crystals characterized by moderate hole mobility $(\mu > 0.05$ cm$^2$ V$^{-1}$ s$^{-1})$, individual merocyanines are organized in one-dimensional (1D) columns or 2D brickwork-type architectures. The latter allows the molecules to minimize their steric interactions, by adopting a shifted anti-parallel dipole–dipole configuration, and at the same time to maximize the electronic overlap between neighbouring units, leading to efficient charge percolation pathways.[14] By optimizing the casting conditions to form extended single-crystalline domains, the highest hole mobility of a merocyanine was measured in a single-crystal Organic Field Effect Transistor (SC-OFET), resulting in about 1 cm$^2$ V$^{-1}$ s$^{-1}$.[15]

Despite a massive number of experimental investigations, only limited computational studies aiming at understanding the charge transport properties of merocyanines can be found in literature. A prominent work was provided by Brückner *et al.*[30,31] By combining a variety of methods, encompassing valence bond self-consistent field (VBSCF), density functional theory (DFT), coupled-cluster (CC) and time-dependent TD-DFT, they correlated the charge reorganization energies to the molecular structure of few merocyanines. Their molecular geometry can in fact be described as a linear combination of two resonant forms, the polyenic (neutral) and the zwitterionic (charge transfer) configurations.[1] It was found that the intra-molecular charge reorganization energy is minimized at the cyanine limit, where both polyenic and zwitterionic configurations are equally weighted in the description of the ground state electronic structure, resulting in a geometry with a vanishing bond length alternation (BLA).[8]

Such pioneering work[30] remains, to the authors' knowledge, one of the few computational studies attempting to rationalize the charge transport properties of merocyanines, though on the basis of a single-molecule parameter. Despite its relevance, the study does not report any mechanistic insights attempting to describe the charge transport processes of merocyanines in general, namely by modelling intra- and inter-molecular mechanisms,[32,33] and by comparing different crystal structures in order to draw general structure–property relationships for such class of highly dipolar organic materials.

Aiming at filling this gap in understanding, we performed a comprehensive computational analysis evaluating both intra- and inter-molecular charge transport parameters for an extended library of merocyanines, altogether six families of molecules were chosen to cover various combinations of D/A groups. The systems were selected amongst the latest experimental literature, reflecting merocyanines with optimized opto-electronic properties.[15,22,25,28] Inspired by the experimental work by Liess *et al.*,[28] within a given class of D/A units, different side groups were also investigated (*e.g.*, alkyl chains *vs.* saturated ring), thus expanding the spectrum of the structures analysed.

We draw clear structure–property relationships, by connecting the solid-state packing motifs with respect to their charge diffusion pathways. Our findings support recent experimental data reporting the highest single crystal hole mobility measured so far ($>1$ cm$^2$ V$^{-1}$ s$^{-1}$) for a certain class of merocyanines.[15] Furthermore, from our computational analysis an alternative class of D/A merocyanine emerged as potential candidate for scoring high (single-crystal) hole mobilities exceeding 1 cm$^2$ V$^{-1}$ s$^{-1}$.

## 2. Computational methods

DFT calculations were performed using the range separated hybrid functional ωB97X-D3 and the polarized Pople split-valence triple-zeta 6-311G** basis set with diffusion and polarisation functions. Both gas phase and solvent calculations were carried out, the latter within the polarizable continuum model approach (PCM) considering as solvents: THF, chloroform, acetone and DMSO. The constrained DFT (C-DFT) calculations were performed by using the CAM-B3LYP functional with D3 dispersion and the 6-311G** basis set. Details concerning the calculations and the codes used are reported in ESI.†

Neutral ground state calculations were performed at the restricted DFT level, while calculations of the charged states were performed at the spin-polarized unrestricted (UDFT) level. Charged states were optimized both in gas and solvents environments.

Internal reorganization energies ($\lambda_i$) were computed both *via* the adiabatic potential approach (four points method) and by evaluating the vibrational normal mode contributions *via* the determination of the Huang–Rhys (HR) factors (for details see ref. 34 and ESI†).

**10852** | *J. Mater. Chem. C*, 2021, **9**, 10851–10864

This journal is © The Royal Society of Chemistry 2021

Charge transfer integrals ($V_{ij}$) were computed at the DFT level ($\omega$B97X-D3/6-311G**) according to the dimer approach and one-electron approximation, as reported in ref. 34 and 35.

Charge transfer rates ($k_{eT}$) were evaluated using the semi-classical Marcus (1) and Marcus-Levich-Jortner (MLJ) (2) formulations.[34,36–39]

The Marcus formula (1) reads:

$$k_{eT} = \frac{2\pi}{\hbar} V_{ij}^2 \frac{1}{\sqrt{4\pi\lambda k_B T}} \exp\frac{-\left(\Delta G^0 + \lambda\right)^2}{4\lambda k_B T} \qquad (1)$$

with $V_{ij}$ the coupling integrals, $\lambda$ the total reorganization energy as the sum of the internal and external contributions ($\lambda_i + \lambda_0$) being $\lambda_0$ set to 0.05 eV if not explicitly computed, $\Delta G^0$ the Gibbs free energy (set to zero for a homogeneous charge transfer reaction, $M^c + M^0 \rightleftarrows M^0 + M^c$), $k_B$ the Boltzmann constant and $T$ the temperature. The MLJ formula (2) reads:

$$k_{eT} = \frac{2\pi}{\hbar} V_{ij}^2 \frac{1}{\sqrt{4\pi\lambda_{0+classic}k_B T}} \qquad (2)$$

$$\sum_{\nu=0}^{\infty} \left[ \exp(-S_{eff})\frac{S_{eff}^\nu}{\nu!} \exp\left(-\frac{(\Delta G^0 + \lambda_{0+classic} + \nu\hbar\omega_{eff})^2}{4\lambda_{0+classic}k_B T}\right) \right]$$

where the quantum description of the non-classical degrees of freedom is represented by a single effective mode of frequency ($\omega_{eff}$) and associated HR factor ($S_{eff}$) determined from the all set of computed HR factors (see Table S16, ESI†). Following previous works[34,39,40] the contributions below *ca.* 150–200 cm$^{-1}$ were not included in the evaluation of $\omega_{eff}$, because at room temperature these frequency vibrations can be described to a good approximation in classical terms and due to their possible anharmonicity. The exceeding classical contributions were summed to $\lambda_0$ and the total contribution reads $\lambda_{0+classic}$ in (2).

Charge carrier mobilities ($\mu$) were computed *via* kinetic Monte-Carlo (kMC) simulations considering both the Brownian diffusion scheme (yielding the zero-field mobility($\mu^0$)) as well as application of an external electric field $E$ (yielding the field-dependent mobility ($\mu(E)$)), often in the theoretical context referred to as time-of-flight (TOF) simulations due to the fact that in TOF experiments the charge transport is measured in an essentially empty density-of-states (DOS).[12] $\mu^0$ was determined by computing the diffusion coefficient $D$ with a set of kMC simulations.[39,40] An approximately linear dependence of the mean square displacement (MSD) of the charge $\langle [r(t) - r(0)]^2 \rangle$ as a function of time $t$ was obtained by averaging over the subsets of 1000 kMC trajectories. The diffusion coefficient $D$ was obtained from the fitted linear dependence of MSD employing the Einstein's eqn (3):

$$D = \lim_{t\to\infty}\left(\frac{MSD}{6t}\right) \qquad (3)$$

The charge mobility was obtained by the Einstein–Smoluchowski's eqn (4):

$$\mu = \frac{eD}{k_B T} \qquad (4)$$

In the presence of an electric field, $\mu(E)$ was computed *via* eqn (5) by applying an electric field $E$ of magnitude $10^5$ V cm$^{-1}$

(voltage of 1 Volt applied on a film with a thickness of 100 nm, *i.e.* corresponding to typical experimental conditions):

$$\mu = \frac{d_f}{\tau E} \qquad (5)$$

where $d_f$ is the distance traveled by the charge in the direction of the applied electric field, and $\tau$ is the time required to travel the distance $d_f$. For specific details about the kMC scheme we refer to ref. 40. kMC charge propagations were performed for a temperature of 300 K, and each trajectory consisted of $10^5$ steps. For the Brownian simulations five subsets of 1000 trajectories each, were run. The field vector for computing $\mu(E)$ was rotated in steps of 15° in the planes perpendicular to the three crystallographic unit cell vectors, respectively. For each step, 100 trajectories were run, and the distance traveled by the charge in the field direction was set to 0.005 cm.

## 3. Results and discussion

### 3.1. Equilibrium structures and BLA

Fig. 1 shows the chemical structures of the donor (D) and acceptor (A) units investigated in this work. The molecular library is divided into classes, depending on the D/A combinations defining the π-conjugated backbone, namely **D1A1, D1A2, D1A3, D2A1, D2A2** and **D2A3**. The donor and acceptor groups are the following: **D1** – 2-amino-thiophene, **D2** – 1-butyl-3,3-dimethylindolin-2-ylidene ('Fischer base'), **A1** – 2-(4-alkylthiazol-2(3H)-ylidene)malonitrile, **A2** – 1,4-dialkyl-3-cyano-6-hydroxy-2pyridone and **A3** – 2-(3-oxo-2,3-dihydro-1H-inden-1-ylidene)malonitrile.

The electron donating strength of the donor groups follows the order **D1** > **D2**, while for the withdrawing scale of the acceptors it is **A1** > **A2** > **A3**. As verified experimentally, the **D1A1** combination features the strongest internal charge-transfer contribution (largest dipole moment) amongst all.[3]
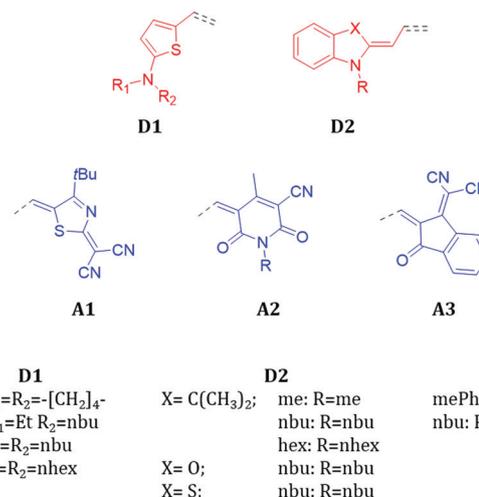


**Fig. 1** Molecular structures of the donor and acceptor units constituting the library of merocyanines investigated in the current work. Details of the various side chains and heteroatoms characterising the D and A units are reported at the bottom.

This journal is © The Royal Society of Chemistry 2021

*J. Mater. Chem. C*, 2021, **9**, 10851–10864 | **10853**

The ground state electronic structure and equilibrium geometry of each merocyanine are determined by the weights of the polyenic (neutral) and zwitterionic (charge transfer) forms (see Scheme 1 for **D1A1**).[30,41,42]

The polyenic *vs.* zwitterionic equilibrium depends on the strength of the D/A groups, on the length of the π-conjugated bridge, and on the environment surrounding the molecule.[1,2,8] Strong D/A units or polar solvents shift the equilibrium towards the zwitterionic form, leading to an intra-molecular charge transfer. Because of such interplay between the resonant forms, the correct description of both ground and excited state structures challenges the majority of standard quantum chemical approaches.[43–45]

It has been shown that for the excited states analysis, time-dependent DFT (TD-DFT) largely overestimates the transition energies, a feature that can be traced back to the lack in DFT of the differential correlation energy between the ground and the excited states.[43,46–49] Double-hybrid functionals (*e.g.*, B2PLYP) seem not to solve the problem, though improving the description of the excited states.[50,51] Remarkable results have been obtained by treating the electron correlation effects *via* quantum Monte Carlo (QMC), Coupled Cluster (CC)[46] or Bethe-Salpeter GW (GW/BSE) methods.[52]

Aiming at an efficient and accurate computational scheme to describe the ground state structure of merocyanines (generally, high dipolar molecules), and recalling the intuitive chemical notion of resonant forms, we used the constrained-DFT (C-DFT) method to optimize the geometry of each molecule, while certain electronic constraints (*i.e.*, partial charges, δ) are applied. C-DFT can be seen as an effective approach to embed external electronic or magnetic perturbations into the electronic structure of a system.[53]

For each merocyanine we tuned the electronic partial charges, as localized on D ($\delta^D$) and A ($\delta^A$) groups, to mimic the polyenic *vs.* zwitterionic forms, and for each $\delta^{D/A}$ value we optimized the corresponding geometry. The polyenic form is thus characterized by $\delta^D = \delta^A = 0q$, while the zwitterionic by $\delta^D = +1.0q$ and $\delta^A = -1.0q$ ($q$ is the electronic charge). In such partitioning scheme, the cyanine limit would be represented by $\delta^D = +0.5q$ and $\delta^A = -0.5q$. Intermediate values for $\delta^D/\delta^A$ lead to differently weighted polyenic *vs.* zwitterionic forms.

For each class of merocyanine we tuned the partial charges by $\pm 0.1q$ ranging from $0.0q$ to $\pm 1.0q$, and we selected the optimized geometries that best reproduce the experimental BLAs, as derived from XRD single crystal diffraction measurements
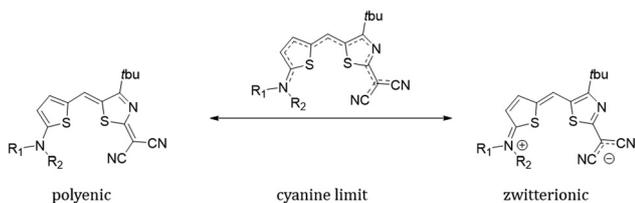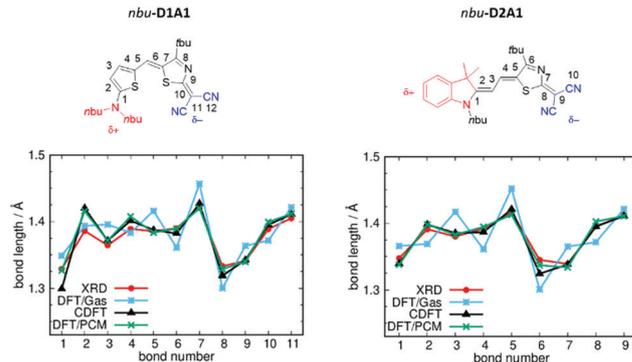


**Fig. 2** Chemical structures and BLA paths (as defined by bond numbering) for *nbu*-**D1A1** (left) and *nbu*-**D2A1** (right) merocyanine – upper panels (*nbu*-**D1A1**, known also as **HB238**).[3] Bond lengths (Å) from XRD data (red lines), DFT (ωB97X-D3/6-311G**, gas phase, blue lines), C-DFT (CAM-B3LYP-D3/6-311G**, gas phase, black lines, $\delta^{D/A} = \pm 0.6q$) and DFT (ωB97X-D3/6-311G**/PCM(DMSO), green lines) calculations – bottom panels.

(XRD, see Table S1 and Fig. S2, ESI† for a comparison between C-DFT BLA patterns by changing $\delta^{D/A}$). Low $\delta^{D/A}$ values ($0.1 \leq \delta^{D/A} \leq 0.4q$) lead to polyenic-like BLA, while high $\delta^{D/A}$ values ($0.7 \leq \delta^{D/A} \leq 1.0q$) lead to zwitterionic-like patterns.

In Fig. 2 are reported the comparisons between the C-DFT ($\delta^{D/A} = \pm 0.6q$), DFT (gas phase) and XRD BLA patterns (see bond numbering) for two representative classes of our library, namely **D1A1** and **D2A1**.

For both merocyanines, the C-DFT structures overlap the experimental ones for almost all bonds by using a $\delta^{D/A} = \pm 0.6q$, thus reflecting a weak zwitterionic character. Slight deviations can be observed at the extremes (*e.g.*, bonds $R^1$ and $R^2$ for **D1A1**, and bond $R^1$ for **D2A1**), being those bonds close to the domains defining the constraints (see details Fig. S1 and S3, ESI†).

The standard DFT calculation (gas phase), in which both a range-separated functional (ωB97X-D3) and a double hybrid functional (B2PLYP) (see Table S3 and Fig. S3, ESI†) were considered to minimize the effects of electron delocalization and self interaction error, largely overestimate the BLA with a pronounced zigzag pattern over all the conjugated path. Notably, **D1A1** and **D2A1** experimental structures are characterized by an almost vanishing BLA in the central part of the molecule (bonds $R^5$–$R^6$–$R^7$ for **D1A1** and $R^2$–$R^3$–$R^4$ for **D2A1**). This is a crucial structural feature, documenting the balanced polyenic *vs.* zwitterionic linear combination in determining a quasi-cyanine structure.

Focusing on the central bonds for each molecule (*e.g.*, $R^5$, $R^6$ for **D1A1** and $R^2$, $R^3$, $R^4$ for **D2A1**), and defining a BLA parameter ($d_{BLA}$) as the difference between single- and double-like bonds (*e.g.*, $d_{BLA} = R^5 - R^6$ for **D1A1** and $R^3 - (R^2 + R^4)/2$ for **D2A1**),[54] it can be seen that for $d_{BLA} > 0$ a polyenic form would be the prevalent resonance structure, while for $d_{BLA} < 0$ a zwitterionic one. Same considerations can be drawn by defining the $d_{BLA}$ as the difference between the average of single and double bonds $\left( d_{BLA} = \sum_i (R^i_{single})/N - \sum_j (R^j_{double})/M \right)$ (see Table S1, ESI†).



**Scheme 1** Polyenic and zwitterionic resonant forms for a representative merocyanine of our study, namely **D1A1**.

**10854** | *J. Mater. Chem. C*, 2021, **9**, 10851–10864

This journal is © The Royal Society of Chemistry 2021

**Table 1** $d_{BLA}$ (Å) values as derived from XRD data, DFT (ωB97X-D3/6-311G**, gas), C-DFT (CAM-B3LYP-D3/6-311G**, $\delta^{D/A}$ = ±0.6$q$) and DFT/PCM (ωB97X-D3/6-311G**, DMSO). For *nbu*-**D1A1** (*i.e.*, **HB238**)[3] four different polymorphs (*nbu*-*P1*/*P4*) were considered (see Section 4 for details)

| Class | Side chain | XRD | DFT (gas) | C-DFT (gas) | DFT/PCM (DMSO) |
|---|---|---|---|---|---|
| **D1A1** | *pyrl* | −0.009 | 0.038 | −0.010 | −0.015 |
| | *et/bu* | −0.012 | 0.039 | −0.010 | −0.013 |
| | *nbu-P1* | −0.003 | 0.038 | −0.010 | −0.013 |
| | *nbu-P2* | −0.010 | | | |
| | *nbu-P3* | −0.023 | | | |
| | *nbu-P4* | −0.013 | | | |
| | *nhex* | −0.017 | 0.039 | −0.010 | −0.013 |
| **D1A2** | *nhex/mePh* | −0.016 | 0.016 | −0.025 | −0.018 |
| **D1A3** | *et* | −0.017 | 0.017 | −0.028 | −0.011 |
| **D2A1** | *nhex* | −0.002 | 0.054 | 0.003 | −0.007 |
| | *nbu* | 0.001 | 0.047 | 0.002 | −0.008 |
| **D2A2** | *me/nbu* | −0.003 | 0.039 | 0.004 | 0.005 |
| **D2A3** | *nbu*(C(CH$_3$)$_2$) | 0.014 | 0.030 | −0.008 | 0.006 |
| | *nbu*(O) | 0.005 | 0.033 | −0.014 | 0.003 |
| | *nbu*(S) | 0.002 | 0.030 | −0.018 | 0.001 |

In Table 1 are reported the experimental and computed $d_{BLA}$. In some cases, as for **D1A1**, **D2A1** and **D2A3** multiple side chains were considered, resulting in different single crystal structures. With exception of **D2A3**, all merocyanines present a $d_{BLA}$ close to zero or negative, showing a *quasi*-cyanine resonant structure slightly unbalanced towards the zwitterionic form.

In the C-DFT scheme $d_{BLA}$ is affected by the choice of $\delta^{D/A}$: for example, for *pyrl*-**D1A1** (see Table S1, ESI†) $d_{BLA}$ varies from 0.064 Å with $\delta^{D/A}$ = ±0.1$q$, to −0.076 Å with $\delta^{D/A}$ = ±1.0$q$. On average, optimized C-DFT structures with $\delta^{D/A}$ = ±0.6$q$ lead to $d_{BLA}$ in good agreement with the experimental data. Small deviations were observed for those cases where $d_{BLA}$ is almost zero. For such cases, best BLAs could be obtained by partial charges ranging from ±0.5$q$ to ±0.7$q$ (see Table S1 and Fig. S3, ESI†).

Notably, by analysing the experimental $d_{BLA}$, we can observe that within a single class, such as **D1A1**, there is a variation of *circa* |0.020| Å just by changing the side groups. Rigid groups (*e.g.*, pyrrolidine, *pyrl*-**D1A1**) or floppy lateral chains (*e.g.*, *n*-hexyl, *nhex*-**D1A1**), affect in different ways the molecular packing (*vide infra*) causing changes in the mutual polarization amongst molecules. Such effect shifts the polyenic *vs.* zwitterionic equilibrium and consequently affects the molecular geometry.

Generally, the unit **D1** induces negative $d_{BLA}$, approaching the cyanine limit for **D1A1**.[2] The **D2** unit results in more positive $d_{BLA}$ than for **D1** (see **D2A3**), showing a more pronounced neutral character,[29] in line with the reduced strength of the donor unit.

Gas phase DFT calculations overestimate the BLA, leading to positive $d_{BLA}$ for all compounds (see Table 1).

As documented in literature,[6,30,41] the polyenic *vs.* zwitterionic forms are affected by solvent/environment effects, and they can be described by a polarizable continuum method (PCM). For the sake of completeness we compared in Table 1 the computed $d_{BLA}$ as derived from DFT/PCM calculations with respect to C-DFT ($\delta^{D/A}$ = ±0.6$q$) and DFT(gas) data.

Within DFT/PCM we considered four solvents with increasing dielectric constants (see ESI,† Table S3), namely chloroform ($\varepsilon$ = 4.71), tetrahydrofuran (THF, $\varepsilon$ = 7.43), acetone ($\varepsilon$ = 20.50) and dimethylsulfoxide (DMSO, $\varepsilon$ = 46.83), as previously documented for some merocyanines (*e.g.*, **D2A2** and *nbu*-**D2A3**).[30] DMSO is usually reported in literature as the solvent that best approximates the polar environment in the solid state.[30,54]

The computed DFT/PCM $d_{BLA}$ show a better match with the experimental values than the DFT(gas) calculations. The $d_{BLA}$ values (see Table 1 and Table S3, ESI†) show the following trend: $d_{BLA}$ becomes negative by increasing the solvent polarity, reflecting an internal charge transfer and favouring the zwitterionic form. For some cases (*e.g.*, **D1A1**), $d_{BLA}$ switches from positive to negative values by increasing $\varepsilon$, showing a polyenic to zwitterionic variation of the structure. Focussing on *pyrl*-**D1A1**, $d_{BLA}$ is varying from 0.007 Å (THF) to −0.015 Å (DMSO). The experimental $d_{BLA}$ (−0.009 Å) would be better caught by acetone (−0.011 Å).

In general, we found that the best match with the experimental data can be achieved either with acetone or DMSO (high $\varepsilon$), for instance for the **D1A1** class, or with chloroform (low $\varepsilon$) as for the case of **D2A3** class (Table 1 and Table S3, ESI†). Unless the dielectric constants of the crystals are known, it appears to be difficult to suggest a *unique* value of $\varepsilon$ to get a reliable and *general* description of $d_{BLA}$ in the solid state. Unambiguously, DFT/PCM improves the description of the BLA pattern with respect to DFT(gas) calculations, and the use of solvents with high $\varepsilon$ leads towards cyanine- or zwitterionic-like structures.

Based on the above comparisons, we suggest C-DFT as an *alternative* embedding method to describe the structure and BLA of highly polar molecules in the solid state, providing results that are in good agreement with experimental XRD data.

The correct prediction of the ground state BLA plays a crucial role in the quantitative evaluation of the charge reorganization energy, as reported in the next session.

### 3.2. Internal hole reorganization energies: a single molecule approach

Merocyanines are p-type semiconductors, therefore the charge carriers to be considered are holes. Generally, a small (<150 meV) hole internal reorganization energy ($\lambda_i^h$) is one of the prerequisites for good charge transport. The internal contribution to $\lambda_i^h$ was evaluated *via* the adiabatic potential method, by following three single-molecule based strategies to describe the structure of the neutral and charged states.

For strategy (i) both neutral and charged states were described by gas phase DFT and (U)DFT calculations; for (ii) the neutral state was described by gas phase C-DFT and the charged by (U)DFT; for (iii) both neutral and charged states were modelled by DFT/ and (U)DFT/PCM.

As discussed previously, the BLA pattern is strongly affected by the choice of the environment or, in C-DFT, by the values of the constrained partial charges. Therefore, the effect of such approaches is, primarily, to displace the potential energy surface (PES) of the neutral ground state from a polyenic to a cyanine- or zwitterionic-like region. As a consequence, strategies (i–iii)

This journal is © The Royal Society of Chemistry 2021

*J. Mater. Chem. C*, 2021, **9**, 10851–10864 | **10855**

**Table 2** Internal hole reorganization energies ($\lambda_i^h$, meV) as computed at the DFT ($\omega$B97X-D3/6-311G**, gas), C-DFT (CAM-B3LYP-D3/6-311G**, $\delta^{D/A} = \pm 0.6q$) and DFT/PCM (DMSO) levels

| Class | Side chain | (i) DFT (gas) | (ii) C-DFT (gas) | (iii) DFT/PCM (DMSO) |
|---|---|---|---|---|
| **D1A1** | *pyrl* | 358 | 127 | 185 |
| | *et/bu* | 361 | 140 | 192 |
| | *nbu* | 355 | 126 | 188 |
| | *nhex* | 366 | 123 | 192 |
| **D1A2** | *nhex/mePh* | 269 | 221 | 213 |
| **D1A3** | *et* | 256 | 278 | 221 |
| **D2A1** | *nhex* | 405 | 177 | 157 |
| | *nbu* | 439 | 177 | 157 |
| **D2A2** | *me/nbu* | 281 | 237 | 156 |
| **D2A3** | *nbu* | 190 | 266 | 163 |
| | *nbu*(O) | 241 | 252 | 173 |
| | *nbu*(S) | 221 | 262 | 183 |

should result in very different internal reorganization energies, given the different energy projections on the neutral and charged PESs.

Table 2 reports the computed $\lambda_i^h$ by comparing strategies (i–iii). Differences amongst $\lambda_i^h$ follow the differences in the neutral ground state BLAs (see Table 1).

DFT(gas) predicts higher (positive) $d_{BLA}$ than C-DFT or DFT/PCM (see Table 1), resulting in high reorganization energies. In fact, DFT(gas) structures are characterized by pronounced BLA in the neutral state (polyenic form) being far from the experimental solid state structures. Upon charging, BLA reverses (see $d_{BLA}$ for the charged state in Tables S2 and S5, ESI†), overall resulting in high $\lambda_i^h$. Such observation is remarkable, pointing out the importance of predicting the correct neutral ground state geometry of merocyanines, due to its impact on the internal charge reorganization energy.

By exploring solvent effects we found that different dielectric constants $\varepsilon$ (*e.g.*, THF, chloroform, acetone, DMSO) lead to different $d_{BLA}$ (Table S3, ESI†), however reflecting similar reorganization energies. For *pyrl*-**D1A1** the computed DFT/PCM $\lambda_i^h$ values are: 189 meV (THF), 202 meV (chloroform), 184 meV (acetone) and 185 meV (DMSO). A factor of six in $\varepsilon$ (7.43 for THF *vs.* 46.83 for DMSO) leads to similar $\lambda_i^h$, though representing different polarizable environments. Within DFT/PCM caution should be taken in the choice of the dielectric constant to be used in the calculation of the neutral ground state structure and reorganization energy.

The class **D1A1** shows the lowest $\lambda_i^h$ (140–123 meV) followed by **D2A1** (177 meV) at the C-DFT level, the latter being the merocyanine with the highest hole mobility ($\mu = 0.11$–$2.34$ cm$^2$ V$^{-1}$ s$^{-1}$) reported in literature.[15] Within the validity of the Marcus theory (*vide infra*) our C-DFT calculations would suggest class **D1A1** as a good candidate for OFET applications as well, showing hole reorganization energy as low as the state-of-the-art **D2A1**. At the DFT/PCM level the situation is slightly different: **D2A1** shows the lowest $\lambda_i^h$ (157 meV), while **D1A1** shows a $\lambda_i^h$ few meV higher (192–185 meV). However, such difference would not affect the charge transport properties in a relevant way.

Classes **D1A3** and **D2A3** show the highest $\lambda_i^h$ at the C-DFT level, suggesting **A3** unit as an unfavourable choice for the minimization of the reorganization energy.

Gas phase DFT values would suggest an opposite trend than C-DFT or DFT/PCM, leading to very large $\lambda_i^h$ values for **D1A1** and **D2A1** (366–358 meV and 439–405 meV). For such reasons, obviously these data are largely overestimated and not representative of the real structural changes occurring upon charging the molecules.

To show the impact of the structural relaxations in affecting the charge reorganization energy of merocyanines, we correlated $\lambda_i^h$ with the variation of $d_{BLA}$ upon charging ($\Delta d_{BLA} = d_{BLA}^{NEUTRAL} - d_{BLA}^{CHARGED}$). Furthermore, for a representative case study, such as *pyrl*-**D1A1**, we calculated $\lambda_i^h$ for different values of the constrained partial charges ($\delta^{D/A}$). Results are collected in Fig. 3.

The parabolic relationship obtained for the C-DFT study by varying $\delta^{D/A}$, see red dots in Fig. 3b, reflects the gradual shift of the neutral ground state geometry from the polyenic ($\delta = 0.2q$) to the zwitterionic ($\delta = 0.8q$) structure, crossing the cyanine region where ideally $\Delta d_{BLA}$ would be close to zero ($\delta \sim 0.6q$) (Fig. 3a). The lowest reorganization energy was obtained for those molecules whose structure in the neutral state is close to the cyanine limit. Class **D1A1** shows the lowest C-DFT reorganization energy (see purple dots and circle in Fig. 3b), minimizing amongst all other classes the $\Delta d_{BLA}$ due to its cyanine-like neutral ground state structure (Table 1)

Our C-DFT approach well matches previous findings (VBSCF and DFT(B3LYP/cc-pVTZ)/PCM calculations),[30] reporting the minimization of the reorganization energy at the cyanine limit.

### 3.3. Internal and external hole reorganization energy: a supramolecular approach

As described in Marcus theory, the total charge reorganization energy ($\lambda$) is the sum of the internal ($\lambda_i$) and external ($\lambda_0$) contributions, the latter resulting from the dynamical response of the environment upon charge transfer.[35] The correct evaluation of $\lambda_0$ would encompass either quantum electrodynamic approaches or quantum mechanical molecular mechanics (QM/MM) methods. Most of the time, and for practical reasons, $\lambda_0$ is
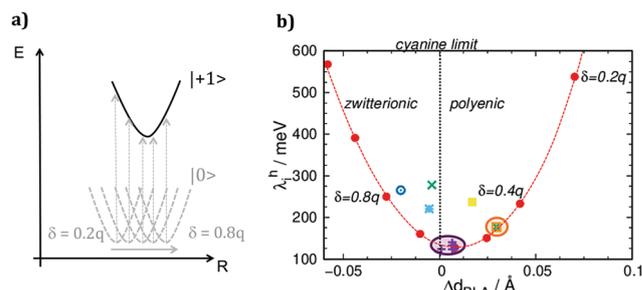


**Fig. 3** (Panel a) Scheme of the potential energy profiles (PEPs) for the neutral and charged states. Multiple PEPs for the neutral ground state mimicking the shift from the polyenic to the zwitterionic structure, as induced by changing $\delta$ in the C-DFT scheme. Vertical arrows sketch the projections on the charged PEP, leading to different final $\lambda_i^h$. (Panel b) C-DFT (CAM-B3LYP-D3/6-311G**) $\lambda_i^h$ for all classes (**D1A1** purple, **D1A2** green, **D1A3** cyan, **D2A1** orange, **D2A2** yellow, **D2A3** blue) as a function of $\Delta d_{BLA}$. In red the computed C-DFT $\lambda_i^h$ for *pyrl*-**D1A1** by changing $\delta^{D/A}$. The cases for $\delta = 0.2$, $0.4$ and $0.8q$ are given for clarity.

**10856** | *J. Mater. Chem. C*, 2021, **9**, 10851–10864

This journal is © The Royal Society of Chemistry 2021

computed *via* continuum approaches[55] or it is considered as an empirical parameter ranging from 0.001 to 0.010 eV. Works by Norton *et al.*[56] and McMahon *et al.*[57] on oligoacenes, reported that the majority of the polarization effects induced by a localised charge, involve the first nearest neighbour molecules.[58]

Inspired by such studies, though aiming at simpler and feasible schemes, we introduced a supramolecular approach combined with the C-DFT method to evaluate both the internal and the external contributions to the reorganization energy. We choose as a prototype case-study for the class of merocyanines *pyrl*-**D1A1**, given its low $\lambda_i^h$ (C-DFT, 127 meV) and its simple crystal structure (*i.e.*, 1D columns of packed anti-parallel molecules, Fig. 4, *vide infra*). We extracted a minimal cluster (*i.e.*, three molecules, *M1M2M3*) from the crystal structure and we optimized the neutral ground state at the DFT level (CAM-B3LYP-D3/6-311G**), by comparing the given BLA patterns for *M1*, *M2* and *M3* with the experimental single crystal data, as reported in Fig. 4. We found that the external molecules *M1* and *M3* are enough to polarize the electronic structure of the central one (*M2*), whose geometry – in turn – relaxes, matching the XRD data (see Fig. 4b). This aspect shows that a minimal cluster like *M1M2M3* can reasonably catch the polarization and inter-molecular effects surrounding *M2*, as occurring in the crystal.

Further, we localized a positive charge (+1*q*) on *M2* and re-optimized the geometry of the entire cluster at the C-DFT level. In such way, by comparing the charged cluster ($M1M2^+M3$) with respect to the neutral one (*M1M2M3*, see Fig. 4c) we could estimate $\lambda_i^h$ and $\lambda_0^h$ *via* simple single point energy calculations. Precisely, $\lambda_i^h$ was computed by extracting the central molecule from the neutral (*M1M2M3*) and charged ($M1M2^+M3$) clusters respectively, and by performing four-single-point calculations for the *M2* and $M2^+$ geometry projections. $\lambda_0^h$ was approximated as the energy contribution coming from the structural deformations and polarizations occurring on *M1* and *M3* upon charge localization on *M2* (see Fig. 4c).
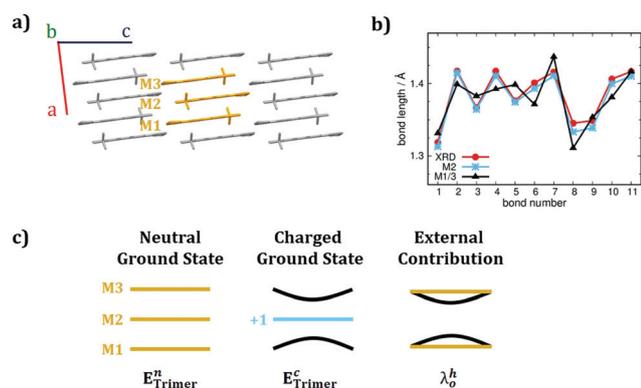


**Fig. 4** (a) *pyrl*-**D1A1** crystal structure on the *ac* crystallographic plane. (b) Comparison between the BLA patterns for *M1/M3* (black) and *M2* (light blue) as computed for the neutral cluster (*M1M2M3*) at the CAM-B3LYP-D3/6-311G** level and the XRD experimental data (red). (c) Scheme for the origin and calculation of $\lambda_0^h$.

With such simple C-DFT supramolecular approach the computed $\lambda_i^h$ and $\lambda_0^h$ for *pyrl*-**D1A1** resulted to be 90 and 25 meV, respectively. $\lambda_i^h$ found with the supramolecular approach is lower than that derived with the single molecule approach (Table 2), regardless C-DFT (127 meV) or DFT/PCM (185 meV) methods are considered. There are no experimental data to corroborate our findings, however the good match between the experimental BLAs and the C-DFT approaches (both single molecule and supramolecular) indirectly suggests that reasonable values for the hole internal reorganization energy of *pyrl*-**D1A1** should lie between 90 and 130 meV.

The computed value for the $\lambda_0^h$ contribution is in very good agreement with literature data as derived from crystalline oligoacenes (1–10 meV) or disorder organic semiconductors (*e.g.*, Alq$_3$, 24 meV).[35,57]

The C-DFT single molecule and supramolecular approaches here proposed are both valuable tools to derive the structure and the reorganization energy of push–pull dyes in the solid state.

### 3.4. Electronic couplings analysis for D1A1 and D2A1 single crystals

To understand the role played by different supramolecular architectures on the charge transport properties in merocyanine single crystals, we modelled the hole transfer processes *via* a combined use of electron transfer theories and kMC simulations (see Computational methods, eqn (1)–(5) and Tables S6–S12, ESI†).[37,59–61]

Firstly, we focused the analysis on the class **D1A1**, because these merocyanines feature one of the lowest hole reorganization energy (see Table 2 and Fig. 3), potentially leading to high hole mobilities. Further, we considered **D2A1** as it shows the highest hole mobility measured on a single crystal OFET (0.11 up to 2.34 cm$^2$ V$^{-1}$ s$^{-1}$).[15] Crystal structures are available in the literature,[28] as well as additional ones were determined in the current work.

The crystal structures we considered involve **D1A1** featuring different side groups, namely pyrrolidone ring (*pyrl*-), ethyl/butyl alkyl chains (*et/bu*-), and *n*-hexyl (*nhex*-).[28] For the case of *n*-butyl chains (*nbu*-**D1A1**, reported also under the name **HB238**)[3] three polymorphic crystals (*Pn*) were here studied and derived by changing the casting solvent (see Table S3, ESI†) or the XRD temperature.[28] Such polymorphs were labeled as: (i) *nbu-P1*, obtained from chloroform and XRD at room temperature; (ii) *nbu-P2*, like *nbu-P1* but XRD at low temperature (100 K); (iii) *nbu-P3*, from mesitylene and XRD at 100 K. A fourth polymorph of *nbu*-**D1A1** was already reported by Liess *et al.*,[28] here named *nbu-P4*-**D1A1**. We focused the analysis on the new found polymorphs (*P1–P3*), details concerning the coupling integrals, the computed charge trajectories and mobilities for *P4* are included in the ESI† (see Table S17, ESI†). An overview of all *nbu-Pn*-**D1A1** polymorphs is reported in Fig. 5.

The impact different polymorphs might have in affecting the charge transport properties becomes clear from Fig. 5. We can speculate that, by considering a typical OFET architecture with the substrate set along the *c*-axis (Fig. 5, blue axis) and the
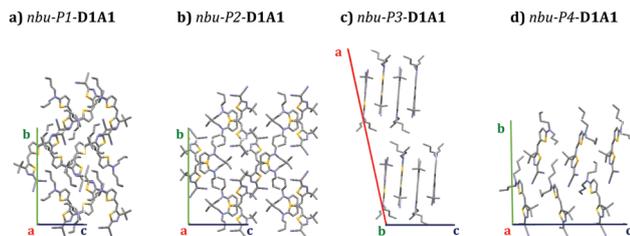
This journal is © The Royal Society of Chemistry 2021

*J. Mater. Chem. C*, 2021, **9**, 10851–10864 | **10857**

**Fig. 5** Crystal structures (supercell) of *nbu-Pn-*D1A1 polymorphs as obtained in the current work, namely (a) *nbu-P1-* (chloroform, XRD at room temperature), (b) *nbu-P2-* (chloroform, XRD at 100 K), (c) *nbu-P3-*D1A1 (mesitylene, XRD at 100K); (d) *nbu-P4-*D1A1 as reported in ref. 28.

molecules lying according to an edge-on configuration, the charge carrier mobility would differ depending on the polymorph constituting the thin film. Presumably, *nbu-P3-*D1A1 would be the case amongst all with the most favorable charge transport, featuring molecules with a nearly perfect edge-on orientation with respect to the substrate (see *bc*-plane Fig. 5).

Overall, we modelled the charge transport for seven crystals belonging to the D1A1 class, precisely: *pyrl-*, *et/bu-*, *nbu-P1*, *nbu-P2*, *nbu-P3-*, *nbu-P4* and *nhex-*D1A1. Experimental data on the charge mobility of D1A1 are only available for amorphous and poly-crystalline thin films, whereas investigations on single crystals do not yet exist. To check the quality of our computational approach and quantitatively compare the computed charge mobility with experimental data, we modelled the charge transport also for the

D2A1 class, where SC-OFET measurements exist, yielding to the highest mobility for merocyanines (average value 0.87 cm$^2$ V$^{-1}$ s$^{-1}$).[15]

**3.4.1. D1A1 class.** The bulkiness and flexibility of the side groups have a remarkable impact on the molecular packing of merocyanines.[29] Due to the high dipole moment ($\sim$10–15 D), all molecules tend to assemble in anti-parallel configurations, however the steric hindrance induced by the lateral groups can cause shifts/rotations of the molecular planes, resulting in packing structures which are far from the ideal centro-symmetric geometry. This is the case for the asymmetric (*et/bu-*) or symmetric (*nbu-* and *nhex-*) alkyl chains, given their major flexibility and steric hindrance in contrast to the rigid *pyrl-*group.[21] *et/bu-* and *nhex-*crystals are characterised by slipped or rotated columns. On the contrary, *pyrl-* induces a tight centro-symmetric packing of the molecules, leading to crystals made by *quasi* 1D columns (see Fig. 6a and Fig. S4, ESI†).[14,22]

Given such variability, the D1A1 class shows a wide spectrum of possible crystals, spanning from 1D columns (*pyrl-*D1A1) to 2D brickwork-type packing (*nbu-P3-*D1A1), representing an ideal case-study to correlate the structure to the charge transport properties for single crystals.

Different packing motifs and dimers featuring significant electronic coupling integrals (*i.e.*, $V_{ij} > 10$ meV) are shown in Fig. 6. Table 3 collects the computed coupling integrals, transfer rates $k_{eT}$ and hole mobility $\mu$ (*vide infra*) for D1A1 and D2A1 classes.

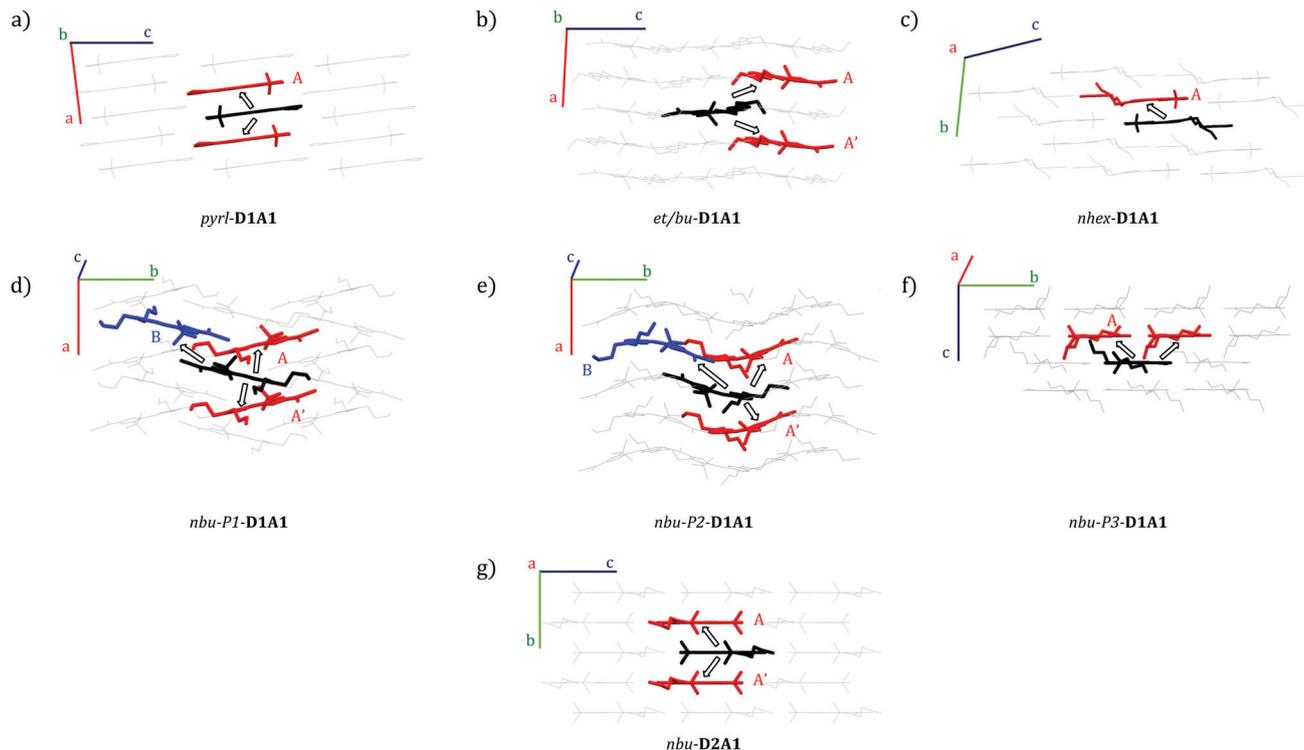*pyrl-*D1A1 crystal is characterised by 1D columns with high intra-column and weak inter-column interactions



**Fig. 6** Supercells of the crystal structures for D1A1 (a–f) and D2A1 (g) classes. For each crystal (a − *pyrl-*, b − *et/bu-*, c − *nhex-*, d − *nbu-P1-*, e − *nbu-P2-*, f − *nbu-P3-*D1A1, g − *nbu-*D2A1) is reported a schematic view of the charge pathways from the central molecule (black) to those nearest neighbor molecules (red) showing large $V_{ij}$ ($V_{ij} > 10$ meV). For *nbu-P2-* and *nbu-P1-*D1A1 crystals (d and e), the molecule highlighted in blue represents, together with the black one, dimer B (see text), namely the inter-column coupling (see text). Letters (A, A′ and B) label non-equivalent nearest neighbor dimers.

**10858** | *J. Mater. Chem. C*, 2021, **9**, 10851–10864

This journal is © The Royal Society of Chemistry 2021

(see Fig. 6a and Fig. S4, ESI†). The intra-column coupling (dimer A, central molecule in black, nearest neighbor in red, Fig. 6) is 56 meV (see Table 3). The inter-column couplings are very low (<2 meV, see Table S6, ESI†). From here, we can already state the charge percolation pathway will mainly occur within single columns (Fig. 6a), rather than from one column to the other, therefore, it is expected to be highly anisotropic (1D).

In the case of *et/bu*-**D1A1**, molecules organize in a brickwork type arrangement, along which the couplings are moderate ($V_{ij}$ = 18 and 14 meV, see the two dimers A and A′ Fig. 6b and Table 3). $V_{ij}$ of the remaining nearest neighbor pairs are below 6 meV (see Table S7, ESI†). The main percolation pathway will occur in a 2D zigzag pattern. Long alkyl chains as in *nhex*-**D1A1** cause a sliding between π–π stacked molecules, leading to *isolated* dimers, with $V_{ij}$ of 23 meV (see dimer A in Fig. 6c and Table 3). All other couplings are below 8 meV (see Table S8, ESI†).

From such analysis we can infer that there is not a smooth and continuous pathway for the charge transport in *nhex*-**D1A1** single crystal. The charge will *reside* on dimer A for several hops before it will advance further along other nearest neighbors. Such temporary trapping will globally decrease the charge mobility, as was previously shown for some perylene bis-imide derivatives.[39,62]

Quite different than *et/bu*- and *nhex*-is the symmetric *nbu*-**D1A1** species (**HB238**). For both *nbu-P1* and *nbu-P2* crystals, the molecules are rotated by 90° forming a *quasi* 1D column to best accommodate the lateral chains (see Fig. 6d and e). The couplings within a column are rather similar for both crystals, being 15 and 20 meV for *nbu-P2* (dimers A and A′, Fig. 6e and Table 3), and 14 meV for *nbu-P1* (dimer A, Fig. 6d and Table 3).

The two crystals however show a different distance between neighboring columns, resulting in different inter-columnar couplings. Such interaction is represented by dimer B (see black–blue molecular pair, Fig. 6d and e).

For *nbu-P2*, dimer B has a higher $V_{ij}$ (50 meV) than in *nbu-P1* (10 meV). The reason for that is because the overlap between the two molecules (Fig. 6d and e) is higher in *nbu-P2* than *nbu-P1*.

The charge transport in *nbu-P2* single crystal should therefore occur *via* alternating jumps between and within the columns, forming an interconnected 2D network. In *nbu-P1* instead the inter-column coupling (dimer B, $V_{ij}$ = 10 meV) is comparable to the intra-column one (dimer A, $V_{ij}$ = 14 meV), possibly leading to a charge transport that would be more isotropic than *nbu-P2*.

For the third crystal polymorph of *nbu*-species (*i.e.*, *nbu-P3*-**D1A1**), molecules form layers of anti-parallel shifted dimers with molecular planes rotated by *circa* 45° (see Fig. 6f). The highest coupling (dimer A, $V_{ij}$ = 35 meV) is lower than that of *nbu-P2* (Table 3). All remaining couplings are below 8 meV (see Table S11, ESI†). Based on such analysis, the most probable charge percolation pathway for *nbu-P3* will be along shifted molecules, forming a 2D brickwork pattern. The fourth polymorph *nbu-P4*-**D1A1** shows the highest coupling similar to *P3* ($V_{ij}$ = 36 meV, see Table S17, ESI†).

**3.4.2. D2A1 class.** **D2A1** class shows overall lower $V_{ij}$ than **D1A1**, with the highest values of 11 and 16 meV for shifted anti-parallel dimers, in agreement with previous investigations.[15] Such dimers form 1D columns similarly to *pyrl*-**D1A1** (see Fig. 6g and Table 3). Due to the presence of *n*-butyl alkyl chains the molecules are more displaced than *pyrl*-**D1A1**, forming a *quasi*-2D brickwork-like arrangement (even though less pronounced as in the case of *nbu-P3* or *et/bu*-**D1A1**). All other remaining couplings are below 4 meV (see Table S12, ESI†).

## 3.5. Kinetic Monte Carlo simulations of charge-carrier mobility

The analysis of the electronic couplings for different merocyanine single crystals suggests peculiar charge transport directions depending on the supramolecular architecture. Therefore, we evaluated the hole transport by computing the transfer rates $k_{eT}$ and the charge carrier mobilities (both $\mu^0$ and $\mu(E)$) *via* kinetic Monte-Carlo (kMC) simulations (see Computational Methods).

**3.5.1. Zero-field mobility ($\mu^0$): D1A1 class.** For *pyrl*-**D1A1** the highest $k_{eT}$ (2.2 × 10$^{13}$ s$^{-1}$) is intra-column, exceeding by three orders of magnitude the inter-columnar transfer rate (3.3 × 10$^{10}$ s$^{-1}$) (see Table S6, ESI†). The charge transport is anisotropic (1D) as evident from the kMC trajectories in Fig. 7a, leading to $\mu^0$ = 0.718 cm$^2$ V$^{-1}$ s$^{-1}$ along the *a*-axis.

The transfer rates for *nhex*-**D1A1** and *et/bu*-**D1A1** crystals is an order of magnitude (∼10$^{12}$ s$^{-1}$) lower than *pyrl*-**D1A1**. Furthermore, in *nhex*-**D1A1** during the kMC charge propagation, the charge resides on dimer A for several hops, as all other possible transfers show kinetic constants one order of magnitude lower (see Table S8, ESI†). This trapping effect reduces the final diffusion length of the charge, hence the mobility.[39,62]
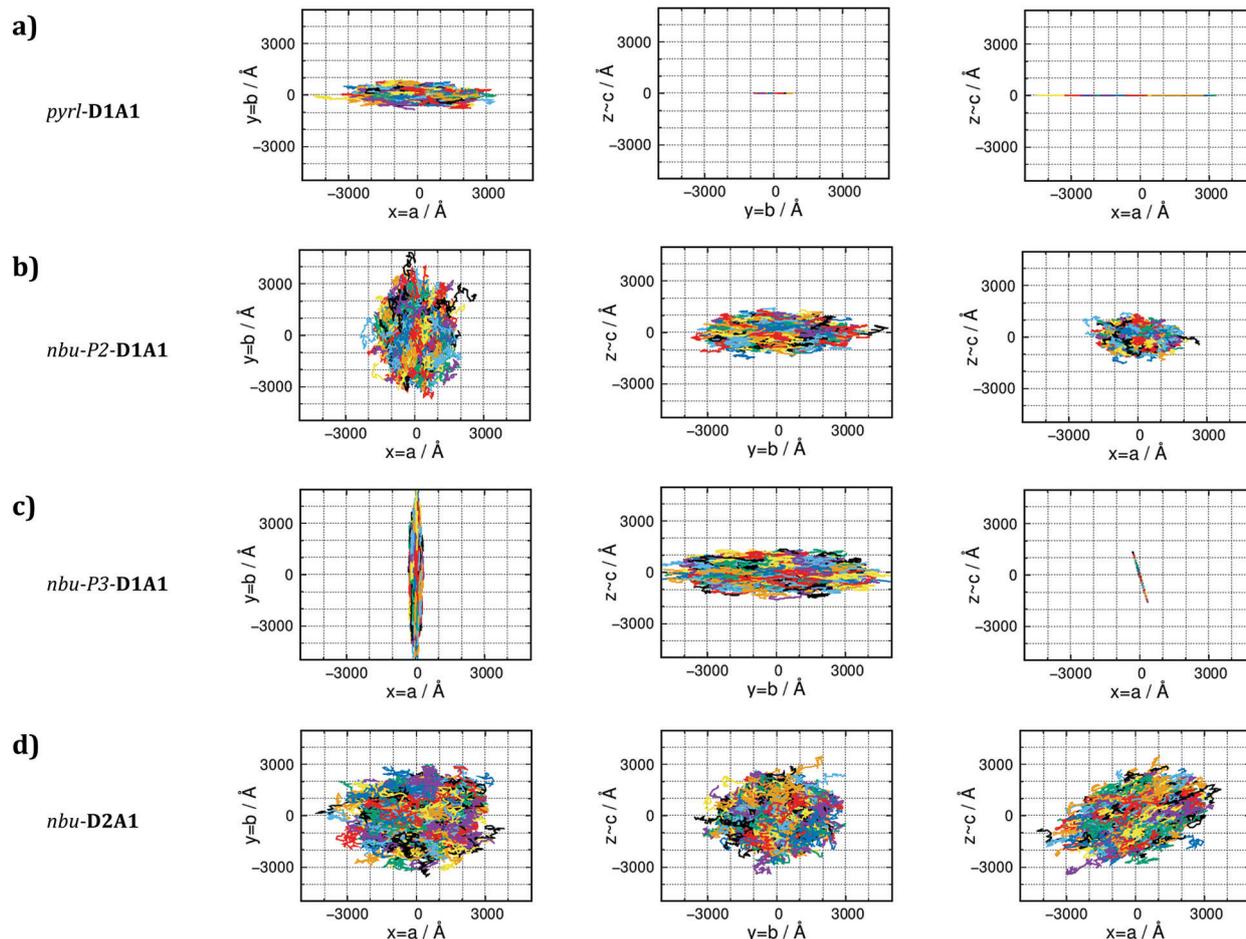
**Table 3** Computed (ωB97X-D3/6-311G\*\*) charge transfer integrals ($V_{ij}$, meV), centre of mass (CoM, Å), and transfer rates ($k_{eT}$ – Marcus theory, s$^{-1}$), for each dimer belonging to the **D1A1** and **D2A1** class. Computed charge mobilities (averaged values, *i.e.* 1/3Tr(**μ**) with **μ** the mobility tensor) evaluated by assuming a Brownian diffusion mechanisms *via* the Einstein–Smoluchowski equation ($\mu^0$, cm$^2$ V$^{-1}$ s$^{-1}$), and an application of an electric field ($\mu(E)$, cm$^2$ V$^{-1}$ s$^{-1}$, $E$ = 10$^5$ V cm$^{-1}$). The MLJ approach was adopted for the calculation of the final charge mobilities

| | Dimer | $|V_{ij}|$ (meV) | CoM (Å) | $k_{eT}$ (s$^{-1}$) | $\mu^0$ (cm$^2$ V$^{-1}$ s$^{-1}$) MLJ | $\mu(E)^b$ (cm$^2$ V$^{-1}$ s$^{-1}$) MLJ |
|---|---|---|---|---|---|---|
| **D1A1** | | | | | | |
| *pyrl* | A | 56 | 3.64 | 2.2 × 10$^{13}$ | 0.718 | 2.075 |
| *et/bu* | A | 14 | 8.43 | 1.3 × 10$^{12}$ | 0.131$^a$ | 0.227$^a$ |
| | A′ | 18 | 8.70 | 2.0 × 10$^{12}$ | | |
| *nbu-P1* | A | 14 | 5.09 | 1.5 × 10$^{12}$ | 0.162 | 0.245 |
| | B | 10 | 10.44 | 6.6 × 10$^{11}$ | | |
| *nbu-P2* | A | 20 | 4.95 | 3.0 × 10$^{12}$ | 0.506 | 1.126 |
| | A′ | 15 | 5.05 | 1.7 × 10$^{12}$ | | |
| | B | 50 | 10.27 | 1.9 × 10$^{13}$ | | |
| *nbu-P3* | A | 35 | 6.60 | 9.0 × 10$^{12}$ | 0.623 | 1.936 |
| *nhex* | A | 23 | 6.34 | 3.9 × 10$^{12}$ | 0.366 | 0.803 |
| **D2A1** | | | | | | |
| *nbu* | A | 16 | 6.26 | 1.0 × 10$^{12}$ | 0.091 | 0.151 |
| | A′ | 11 | 6.26 | 4.9 × 10$^{11}$ | | |

$^a$ Cut-off in Huang–Rhys analysis at 200 cm$^{-1}$. $^b$ The largest computed $\mu(E)$ is reported.

This journal is © The Royal Society of Chemistry 2021

*J. Mater. Chem. C*, 2021, **9**, 10851–10864 | **10859**

**Fig. 7** Plot of 1000 kMC trajectories (each consisting of $10^5$ steps) for each **D1A1** and **D2A1** class (from top to bottom: *pyrl*-, *nbu-P2*-, *nbu-P3*-**D1A1** and *nbu*-**D2A1**). Trajectories are reported for the three Cartesian planes, namely *yx*, *zy* and *zx* (crystallographic axes are reported as well).

The variations in the kinetic constants reflect the differences in the crystal structures: *et/bu*- and *nhex*-**D1A1** show less packed structures than *pyrl*-**D1A1**, leading overall to lower $\mu^0$ for *et/bu*- (0.131 cm$^2$ V$^{-1}$ s$^{-1}$) and *nhex*- (0.366 cm$^2$ V$^{-1}$ s$^{-1}$) (Table 3).

For the *n*-butyl species (*nbu-Pn*-**D1A1**, *i.e.*, **HB238**), the room-temperature polymorph *nbu-P1*-shows transfer rates of $\sim 10^{12}$ s$^{-1}$, resulting in $\mu^0$ of 0.162 cm$^2$ V$^{-1}$ s$^{-1}$. This value is comparable to *et/bu*-**D1A1**. On the contrary, for the other polymorphs *nbu-P2*- and *nbu-P3*- the computed averaged $\mu^0$ raises, approaching the value of *pyrl*-**D1A1** (0.718 cm$^2$ V$^{-1}$ s$^{-1}$): $\mu^0$ = 0.506 cm$^2$ V$^{-1}$ s$^{-1}$ for *nbu-P2*-, 0.623 cm$^2$ V$^{-1}$ s$^{-1}$ for *nbu-P3*-. The charge mobility increases from *nbu-P1*- to *nbu-P2/P3*-**D1A1**. This increment is because the percolation pathway along the inter-column direction (dimer B, Fig. 6d and e) in *nbu-P2/P3* is switched on due to a higher coupling than *nbu-P1* (50 meV *vs.* 10 meV), leading to higher kinetic constants ($\sim 10^{13}$ s$^{-1}$ *vs.* $\sim 10^{11}$ s$^{-1}$). For *nbu-P2*-**D1A1** the charge can hop both across columns (*via* dimer B) and within a column (*via* dimers A and A′) (Fig. 6e). Such hopping mechanism results in a 2D/3D-like diffusive charge transport (see kMC trajectories in Fig. 7b). For *nbu-P3*-**D1A1** molecules form a brickwork-like pattern, favoring a *continuous* charge percolation pathway across neighboring layers (mainly the *cb* crystal plane, Fig. 7c). For *nbu-P4*-**D1A1**

(see Table S17, ESI†), molecules form a brickwork-like pattern similarly to *P3*, leading to charge percolation pathways in the *cb* plane.

Summarizing the charge transport modeling for **D1A1** class, we found that *pyrl*-, *nbu-P3/P4*-**D1A1** are the merocyanines featuring the highest zero-field hole mobility in single crystals, reaching values approaching 0.6–0.7 cm$^2$ V$^{-1}$ s$^{-1}$ (or exceeding unity, as in the case of *P4*, see Table S17, ESI†). For a comparison between the Marcus and the MLJ values, see (Tables S6–S12 and S10, ESI†). $\mu^0$ overcomes unity if an electric field ($\mu(E)$) was applied (see Table 3). Such values are in good agreement with recent findings by Lv *et al.*, reporting hole mobilities of 0.48–0.60 cm$^2$ V$^{-1}$ s$^{-1}$ in an OFET prepared by vacuum-deposition of diphenylaminothienyl-dicyanovinylthiazol (named **Ph$_2$ATTA**), that is a merocyanine belonging to the **D1A1** class, featuring di-phenyl as side group.[16]

*pyrl*- and *nbu-P3/P4*-**D1A1**, however show very different charge diffusion and percolation mechanisms resulting from their different single crystal structures. For *pyrl*-**D1A1** charge transport is highly anisotropic (Fig. 7a), occurring prevalently in one dimension (intra-column, *a*-axis of the crystal). For *nbu-P3*-**D1A1** (as well as for *P4*, see Table S17, ESI†) charge transport occurs mainly in two-dimensions (Fig. 7c), covering a zigzag trajectory between neighboring layers (Fig. 6f).

**10860** | *J. Mater. Chem. C*, 2021, **9**, 10851–10864

This journal is © The Royal Society of Chemistry 2021

For polymorph *nbu-P2*-**D1A1** holes hop in an alternating pattern across and within columns, the transport being less anisotropic than for *nbu-P3*-**D1A1** (see Fig. 7b).

For asymmetric *et/bu-* or long symmetric *nhex*-**D1A1** species, charge transport is rather disfavored as compared to *pyrl-* and *nbu-* species (though notable hole mobilities are computed, see Table 3). A similar situation occurs for *nbu-P1*-**D1A1** crystal.

**3.5.2. Zero-field mobility ($\mu^0$): D2A1 class.** *nbu*-**D2A1** shows a similar packing structure (*i.e.*, antiparallel dimers) and 1D columns as *pyrl*-**D1A1** (Fig. 6g). The highest kinetic constant is computed for dimers belonging within a column ($k_{eT} = 1.0 \times 10^{12}$ s$^{-1}$), while the inter-columnar transfer rates are two orders of magnitude smaller ($\sim 10^{10}$ s$^{-1}$). In comparison to *pyrl*-**D1A1**, *nbu*-**D2A1** shows intra- *vs.* inter-column rate constants which differ less from each other (see Table S12, ESI†). To note that, not only is the difference in kinetic constants between intra- and inter-columnar transfers smaller in *nbu*-**D2A1** than *pyrl*-**D1A1**, but also the highest computed kinetic constants for *nbu*-**D2A1** ($1.0 \times 10^{12}$ s$^{-1}$ and $4.9 \times 10^{11}$ s$^{-1}$) are significantly smaller than *pyrl*-**D1A1** ($2.2 \times 10^{13}$ s$^{-1}$), leading to an overall low $\mu^0$. The reason for that can be traced back to smaller electronic couplings of *nbu*-**D2A1** as compared to *pyrl*-**D1A1** (16 meV *vs.* 56 meV), as well as a higher reorganization energy (177 meV *vs.* 127 meV).

Such characteristics lead to a more isotropic charge diffusion pathways for *nbu*-**D2A1** than for *pyrl*-**D1A1** (Fig. 7d and a). We can speculate that due to the isotropic nature, charge transport in *nbu*-**D2A1** might be less sensitive to structural disorder at the microscopic level (*e.g.*, poly-crystalline domains, grain boundaries, amorphous regions, structural defects, impurities) than *pyrl*-**D1A1**.

The computed charge mobility for *nbu*-**D2A1** spans from $\mu^0 = 0.091$ cm$^2$ V$^{-1}$ s$^{-1}$ up to $\mu(E) = 0.151$ cm$^2$ V$^{-1}$ s$^{-1}$ (see Table 3), approaching the same order of magnitude of the bottom and averaged charge mobility values as measured on single crystal OFETs, namely 0.11 and 0.86 cm$^2$ V$^{-1}$ s$^{-1}$.[15]

Given the computed charge mobilities, we believe that the **D1A1** class might potentially show superior charge transport properties at the single crystal level than the **D2A1**.

**3.5.3. Field-dependent mobility $\mu(E)$.** The computed $\mu(E)$ values are relatively similar to the Brownian $\mu^0$ (Table 3),[63] which is expected since we considered single crystals, without taking into account amorphous or polycrystalline morphologies, for which a much stronger field dependence would be expected.[13]

To put our findings in perspective and highlight some trends within and between merocyanines, in Fig. 8 we correlated the computed field-dependent charge mobilities of **D1A1** and **D2A1** classes with respect to the experimental ones, the latter either taken from literature or measured in the current work.

For a proper comparison between computed and experimental results, some cautionary notes should be added here. First of all, for the **D1A1** class the experimental data taken from Liess *et al.*[28] were obtained from polycrystalline thin films, while for the **D2A1** experimental data were obtained from single-crystals.[15] Our simulations refer to single crystal samples. Secondly, for both

cases, OFET mobilities in the linear regime are reported. We should point out that our simulations assume a (field dependent) charge transport in an empty density of state (DOS), a condition which is however only valid in TOF experiments. In an OFET device, on the contrary, the DOS is not empty (due to trap filling induced by applying the gate electric field) and the charge mobility increases by increasing the carrier concentration.[64] The latter effect is not taken into account in our computational treatment. Such differences justify eventual discrepancies between the computed and the experimental charge mobility, besides other factors (*e.g.*, contact resistance, chemical impurities, structural defects) that can not be taken into account in our simulations.

Within the **D1A1** class, both theoretical ($\mu_{theo}(E)$) and experimental ($\mu_{exp}(E)$) mobilities (orange circles, Fig. 8) increase for crystals showing either 1D (*pyrl-*) or 2D (*nbu-P3/P4-*) brickwork-like packing. The experimental data are lower than the theoretical ones, lying below the ideal linear correlation (*i.e.*, single crystal) highlighted by the black dashed line and grey circles in Fig. 8. This discrepancy, as previously mentioned, can be related to the fact that experiments were carried out on poly-crystalline thin films rather than a single crystal.

Further, it is uncertain, whether the crystal structure determined by XRD on a micron-sized crystal is identical to the one realized in an OFET thin film. As here documented, we discovered three new polymorphs (*P1–P3*) of *nbu*-**D1A1** (**HB238**), in addition to the one already reported (*P4*) by Liess *et al.*[28] (see Fig. 5). By combining optical and Atomic Force Microscopy (AFM) investigations, we were able to prove that after thermal
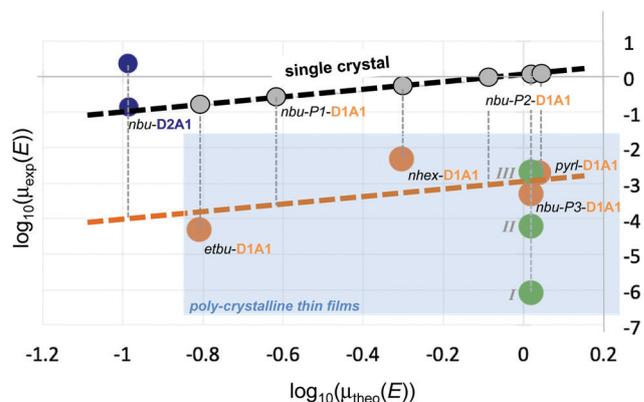


**Fig. 8** Correlation between the experimental and the theoretical single-crystal hole mobilities, $\mu_{exp}(E)$ and $\mu_{theo}(E)$, for **D2A1** and **D1A1** classes. For *nbu*-**D2A1** the lowest and the highest experimental values are reported (blue circles; ref. 15). In the case of **D1A1** class (orange circles; ref. 28), it was assumed that the crystal structure determined by XRD is present in the OFET thin film as well. For *nbu-P3*-**D1A1**, the crystal structure was verified and in addition to published data,[28] the charge mobility was measured on thin films thermally annealed, namely *I* ($T = 50$ °C), *II* ($T = 110$ °C) and *III* ($T = 130$ °C) – green circles. The dashed black line indicates the theoretical limit of the charge mobility by considering single crystal conditions, without the inclusion of thermal oscillations (grey circles). Vertical grey dashed lines represent the assumed variation of the charge mobility due to the polycrystalline morphology. The polycrystalline regime is highlighted in light blue.

annealing the *nbu*-**D1A1** molecules assume an edge-on orientation in thin films (see Fig. 5), independently of the substrate [L. Böhner *et al.*, unpublished data], and we could demonstrate that this corresponds to polymorph *nbu-P3* (*i.e.* a crystalline structure which differs from the one reported in Liess *et al.*[28]).

To stress the impact of the thin-film morphology, the charge carrier mobility was measured in this work for *nbu-P3*-**D1A1** over a series of thin films annealed at different temperatures (see green circles for *nbu*-**D1A1**, Fig. 8). By increasing the annealing temperature, the crystallinity (crystal size) increases, rising $\mu_{exp}(E)$ by four orders of magnitude (from $8.57 \times 10^{-7}$ cm$^2$ V$^{-1}$ s$^{-1}$ initial pristine state **I**, to $2.1 \times 10^{-3}$ cm$^2$ V$^{-1}$ s$^{-1}$ final annealed state **III**). We may speculate that, if (i) a single-crystal OFET were to be prepared similar to the one reported for **D2A1**,[15] and if (ii) the orientation of the *nbu*-**D1A1** single crystal were such, that the crystal axis featuring the largest hole mobility (*b*-axis, see Fig. 5c and 7c and Table S16, ESI†) would coincide with the electric field vector, the expected experimental charge mobility of *nbu*-**D1A1** might reach the theoretical range of 0.2–2 cm$^2$ V$^{-1}$ s$^{-1}$ (Table 3), as computed for a single crystal. An indirect evidence of such high mobility values for the **D1A1** class (*e.g.*, $> 0.1$ cm$^2$ V$^{-1}$ s$^{-1}$) can be already found in literature for the merocyanine **Ph$_2$ATTA**. For such case, the experimental charge mobility increases by orders of magnitude, from $2.4 \times 10^{-3}$ cm$^2$ V$^{-1}$ s$^{-1}$ for solution processed thin films, up to 0.48–0.6 cm$^2$ V$^{-1}$ s$^{-1}$ for vacuum-deposited layers.[16]

Notably, the computed $\mu(E)$ for the **D2A1** class (0.151 cm$^2$ V$^{-1}$ s$^{-1}$) is in good agreement with the one measured on single crystals,[15] as evident from Fig. 8 (see blue circles representing the lowest and highest $\mu_{exp}(E)$ for *nbu*-**D2A1**, namely 0.11 and 2.34 cm$^2$ V$^{-1}$ s$^{-1}$, respectively).

However, the maximum experimental mobility (2.34 cm$^2$ V$^{-1}$ s$^{-1}$) exceeds the computed one by more than one order of magnitude.[15] A possible reason for such underestimation could be the anisotropy of the charge transport, whereas we reported average values. However, this could account for a factor of 3 at best, and as can be seen in Fig. 7d charge transport within the **D2A1** crystal is isotropic. Among other possible reasons, we attribute a relevant role to the fact that we have computed the charge mobility by considering *static* crystal structures, namely by neglecting the impact of thermal motions. As documented in literature,[65–67] the electronic couplings are very sensitive to the inter-molecular oscillations as activated by the temperature, therefore small geometrical displacements can lead to huge variations of $V_{ij}$. Usually, thermal effects introduce structural disorder, localizing the polaron over one or few sites and broadening the distribution of the couplings, thus leading to a decrease of the charge mobility.[65] However, for some crystal structures, thermal motions can *open* new charge percolation channels at the molecular scale,[39,68,69] increasing the coupling integrals and rising the charge mobility.[70,71]

To explore such possibility and the effect of small oscillations on the coupling integrals[72] and site energies, we displaced one molecule belonging to the dimer showing the highest coupling

for both *nbu*-**D2A1** and *pyrl*-**D1A1**, along the longitudinal direction (see Fig. S11, ESI†). By considering oscillations within the thermal energy $k_BT$ (25 meV), $V_{ij}$ for *pyrl*-**D1A1** vary from 25 meV to 129 meV (being 56 meV the value at the crystal equilibrium geometry). For *nbu*-**D2A1** $V_{ij}$ vary from few meV up to 79 meV (being 16 meV the value at equilibrium). This first preliminary evaluation shows that the couplings, as well as the charge mobility, might increase for both cases when thermal effects are taken into account. Such aspect can further justify, in first approximation, our underestimation of the single crystal charge mobility for **D2A1** as compared to the maximum experimental value. Further investigations in this direction are currently ongoing.

## 4. Conclusions

We investigated a library of merocyanines by varying the donor (D) and acceptor (A) groups, aiming at modelling their structure and charge transport properties. Following a bottom-up approach, we found that C-DFT is an effective embedding method to quantitatively describe the BLA patterns of mero-cyanines in the solid state. All compounds show cyanine- or zwitterionic-like BLAs, in agreement with XRD data. Such feature is of paramount importance for the prediction of the reorganization energy.

Hole reorganization energies were computed following both the adiabatic (single molecule) method and a supramolecular (cluster) approach. Both schemes provided similar internal contributions ($\sim$90–130 meV), the latter allowing to derive also the external contribution ($\sim$25 meV), otherwise assumed as an empirical parameter. By increasing the strength of the D/A units the reorganization energy decreases for molecules close to the cyanine limit. The lowest value was computed for the **D1A1** class, as derived by coupling the 2-amino-thiophene donor group (**D1**) and the 2-(4-alkylthiazol-2(3*H*)-ylidene)malonitrile acceptor unit (**A1**).

We computed the charge transfer integrals and kMC charge carrier trajectories for a variety of **D1A1** crystals, as obtained either by varying the side groups or by changing the casting conditions. We found that the charge mobility is tremendously affected by tiny variations of the packing structures.

We demonstrated that asymmetric (*e.g.*, ethyl/butyl, *et/bu*-**D1A1**) or long symmetric (*e.g.*, *n*-hexyl, *nhex*-**D1A1**) side groups are detrimental for charge transport, leading to *isolated* dimers where the charge resides during the dynamics, decreasing the mobility.

Small rigid side groups (*e.g.*, pyrrolidine, *pyrl*-**D1A1**) lead to crystals characterised by one-dimensional columns with stacked anti-parallel molecules. The computed charge mobility for *pyrl*-**D1A1** resulted to be high ($> 0.7$ cm$^2$ V$^{-1}$ s$^{-1}$) and anisotropic, being the hole diffusion within the columnar direction.

Symmetric alky chains (*e.g.*, *n*-butyl, *nbu*-**D1A1**, *i.e.* **HB238**) show a balanced situation between rigid (*pyrl*-) and flexible (*et/bu*-, *nhex*-) groups. In addition to the crystal structure

**10862** | *J. Mater. Chem. C*, 2021, **9**, 10851–10864

This journal is © The Royal Society of Chemistry 2021

already reported in literature, three new crystal polymorphs for *nbu*-**D1A1** were discovered by changing the temperature and casting solvents. Generally, the molecules pack in slipped and rotated configurations creating layers of two-dimensional networks. Such arrangement allows the charge transport to be less anisotropic than *pyrl*-**D1A1**, though showing similar high hole mobilities ($<0.6$ cm$^2$ V$^{-1}$ s$^{-1}$). Amongst the four polymorphs of *nbu*-**D1A1**, the computed mobility varies by one order of magnitude, whereas the maximum value is received for a brickwork-like supramolecular architecture.

To strengthen our predictions, we modelled the charge transport for the **D2A1** class, consisting of 1-butyl-3,3-dimethylindolin-2-ylidene as donor (**D2**) unit, coupled with the **A1** group. Such class shows the highest measured charge mobility on a single crystal OFET so far (average value, 0.87 cm$^2$ V$^{-1}$ s$^{-1}$). The computed value (0.151 cm$^2$ V$^{-1}$ s$^{-1}$) matches well the experimental average mobility, validating our modelling scheme and its predictive power. Reasons for the underestimate of the computed mobility might be attributed to the role of electron–phonon couplings, here not taken into account. Indeed, within the hopping regime, molecular vibrations can play a role in enhancing charge transport, leading to a phonon-assisted process possibly raising the computed charge mobility.

Based on our computational investigation we suggest that the **D1A1** class of merocyanines, in particular species having *nbu*- or *pyrl*- side groups, can overtake the state-of-the-art **D2A1**, leading to comparable hole mobilities at the single crystal level, a feature that will be of high relevance for OSCs as well as OFETs.

## Author contributions

L. B., D. H. and J. N. performed the experimental analyses. N. G., F. N., and D. F. performed the computational analyses. N. G., F. N., K. M. and D. F. conceptualized the work. All authors contributed to rationalize the data and write the manuscript.

## Conflicts of interest

There are no conflicts of interest to declare.

## Acknowledgements

## Notes and references

1 S. R. Marder, C. B. Gorman, F. Meyers, J. W. Perry, G. Bourhill, J.-L. Brédas and B. M. Pierce, *Science*, 1994, **265**, 632–635.

2 F. Würthner, G. Archetti, R. Schmidt and H.-G. Kuball, *Angew. Chem., Int. Ed.*, 2008, **47**, 4529–4532.

3 H. Bürckstümmer, E. V. Tulyakova, M. Deppisch, M. R. Lenze, N. M. Kronenberg, M. Gsänger, M. Stolte, K. Meerholz and F. Würthner, *Angew. Chem., Int. Ed.*, 2011, **50**, 11628–11632.

4 S. R. Marder, L.-T. Cheng, B. G. Tiemann, A. C. Friedli, M. Blanchard-Desce, J. W. Perry and J. Skindhøj, *Science*, 1994, **263**, 511–514.

5 V. Parthasarathy, R. Pandey, M. Stolte, S. Ghosh, F. Castet, F. Würthner, P. K. Das and M. Blanchard-Desce, *Chem. – Eur. J.*, 2015, **21**, 14211–14217.

6 F. Würthner, R. Wortmann, R. Matschiner, K. Lukaszuk, K. Meerholz, Y. DeNardin, R. Bittner, C. Bräuchle and R. Sens, *Angew. Chem., Int. Ed. Engl.*, 1997, **36**, 2765–2768.

7 H. Bürckstümmer, N. M. Kronenberg, M. Gsänger, M. Stolte, K. Meerholz and F. Würthner, *J. Mater. Chem.*, 2010, **20**, 240–243.

8 C. B. Gorman and S. R. Marder, *Proc. Natl. Acad. Sci. U. S. A.*, 1993, **90**, 11297–11301.

9 K. Meerholz, B. L. Volodin, Sandalphon, B. Kippelen and N. Peyghambarian, *Nature*, 1994, **371**, 497–500.

10 F. Würthner, R. Wortmann and K. Meerholz, *ChemPhysChem*, 2002, **3**, 17–31.

11 F. Würthner and K. Meerholz, *Chem. – Eur. J.*, 2010, **16**, 9366–9373.

12 H. Bässler and D. Hertel, *ChemPhysChem*, 2008, **9**, 666–688.

13 H. Bässler, *Phys. Status Solidi B*, 1993, **175**, 15–56.

14 A. Liess, L. Huang, A. Arjona-Esteban, A. Lv, M. Gsänger, V. Stepanenko, M. Stolte and F. Würthner, *Adv. Funct. Mater.*, 2015, **25**, 44–57.

15 A. Liess, M. Stolte, T. He and F. Würthner, *Mater. Horiz.*, 2016, **3**, 72–77.

16 A. Lv, M. Stolte and F. Würthner, *Angew. Chem., Int. Ed.*, 2015, **54**, 10512–10515.

17 C. Reese, W.-J. Chung, M.-M. Ling, M. Roberts and Z. Bao, *Appl. Phys. Lett.*, 2006, **89**, 202108.

18 G. Xue, C. Fan, J. Wu, S. Liu, Y. Liu, H. Chen, H. L. Xin and H. Li, *Mater. Horiz.*, 2015, **2**, 344–349.

19 R. Zeis, T. Siegrist and C. Kloc, *Appl. Phys. Lett.*, 2005, **86**, 022103.

20 J. Takeya, M. Yamagishi, Y. Tominari, R. Hirahara, Y. Nakazawa, T. Nishikawa, T. Kawase, T. Shimoda and S. Ogawa, *Appl. Phys. Lett.*, 2007, **90**, 102120.

21 A. Liess, A. Lv, A. Arjona-Esteban, D. Bialas, A.-M. Krause, V. Stepanenko, M. Stolte and F. Würthner, *Nano Lett.*, 2017, **17**, 1719–1726.

22 L. Huang, M. Stolte, H. Bürckstümmer and F. Würthner, *Adv. Mater.*, 2012, **24**, 5750–5754.

23 E. Kirchner, D. Bialas, F. Fennel, M. Grüne and F. Würthner, *J. Am. Chem. Soc.*, 2019, **141**, 7428–7438.

24 D. Bialas, C. Zhong, F. Würthner and F. C. Spano, *J. Phys. Chem. C*, 2019, **123**, 18654–18664.

25 D. Bialas, A. Zitzler-Kunkel, E. Kirchner, D. Schmidt and F. Würthner, *Nat. Commun.*, 2016, **7**, 12949.

26 Y. Li, H. K. M. Sheriff Jr., X. Liu, C.-K. Wang, K. Ding, H. Han, K.-T. Wong and S. R. Forrest, *J. Am. Chem. Soc.*, 2019, **141**, 18204–18210.

27 N. M. Kronenberg, V. Steinmann, H. Bürckstümmer, J. Hwang, D. Hertel, F. Würthner and K. Meerholz, *Adv. Mater.*, 2010, **22**, 4193–4197.

28 A. Liess, A. Arjona-Esteban, A. Kudzus, J. Albert, A.-M. Krause, A. Lv, M. Stolte, K. Meerholz and F. Würthner, *Adv. Funct. Mater.*, 2018, **29**, 1805058.

29 A. Arjona-Esteban, J. Krumrian, A. Liess, M. Stolte, L. Huang, D. Schmidt, V. Stepanenko, M. Gsänger, D. Hertel, K. Meerholz and F. Würthner, *J. Am. Chem. Soc.*, 2015, **137**, 13524–13534.

30 C. Brückner, C. Walter, M. Stolte, B. Braïda, K. Meerholz, F. Würthner and B. Engels, *J. Phys. Chem. C*, 2015, **119**, 17602–17611.

31 C. Brückner and B. Engels, *J. Phys. Chem. A*, 2015, **119**, 12876–12891.

32 C. Brückner, F. Würthner, K. Meerholz and B. Engels, *J. Phys. Chem. C*, 2017, **121**, 4–25.

33 C. Brückner, F. Würthner, K. Meerholz and B. Engels, *J. Phys. Chem. C*, 2017, **121**, 26–51.

34 S. Di Motta, E. Di Donato, F. Negri, G. Orlandi, D. Fazzi and C. Castiglioni, *J. Am. Chem. Soc.*, 2009, **131**, 6591–6598.

35 V. Rühle, A. Lukyanov, F. May, M. Schrader, T. Vehoff, J. Kirkpatrick, B. Baumeier and D. Andrienko, *J. Chem. Theory Comput.*, 2011, **7**, 3335–3345.

36 H. Oberhofer, K. Reuter and J. Blumberger, *Chem. Rev.*, 2017, **117**, 10319–10357.

37 V. Stehr, R. F. Fink, M. Tafipolski, C. Deibel and B. Engels, *Wiley Interdiscip. Rev.: Comput. Mol. Sci.*, 2016, **6**, 694–720.

38 V. Stehr, J. Pfister, R. F. Fink, B. Engels and C. Deibel, *Phys. Rev. B: Condens. Matter Mater. Phys.*, 2011, **83**, 155208.

39 E. Di Donato, R. P. Fornari, S. Di Motta, Y. Li, Z. Wang and F. Negri, *J. Phys. Chem. B*, 2010, **114**, 5327–5334.

40 S. Canola and F. Negri, *Phys. Chem. Chem. Phys.*, 2014, **16**, 21550–21558.

41 A. Capobianco, R. Borelli, A. Landi, A. Velardo and A. Peluso, *J. Phys. Chem. A*, 2016, **120**, 5581–5589.

42 F. Würthner, C. Thalacker, R. Matschiner, K. Lukaszuk and R. Wortmann, *Chem. Commun.*, 1998, 1739–1740.

43 B. Le Guennic and D. Jacquemin, *Acc. Chem. Res.*, 2015, **48**, 530–537.

44 H. Lischka, D. Nachtigallová, A. J. A. Aquino, P. G. Szalay, F. Plasser, F. B. C. Machado and M. Barbatti, *Chem. Rev.*, 2018, **118**, 7293–7361.

45 C. Brückner and B. Engels, *Chem. Phys.*, 2017, **482**, 319–338.

46 R. Send, O. Valsson and C. Filippi, *J. Chem. Theory Comput.*, 2011, **7**, 444–455.

47 H. Zhekova, M. Krykunov, J. Autschbach and T. Ziegler, *J. Chem. Theory Comput.*, 2014, **10**, 3299–3307.

48 B. Moore Li and J. Autschbach, *J. Chem. Theory Comput.*, 2013, **9**, 4991–5003.

49 S. Knippenberg, R. L. Gieseking, D. R. Rehn, S. Mukhopadhyay, A. Dreuw and J.-L. Brédas, *J. Chem. Theory Comput.*, 2016, **12**, 5465–5476.

50 S. Grimme, *J. Chem. Phys.*, 2006, **124**, 034108.

51 S. Grimme and F. Neese, *J. Chem. Phys.*, 2007, **127**, 154116.

52 P. Boulanger, D. Jacquemin, I. Duchemin and X. Blase, *J. Chem. Theory Comput.*, 2014, **10**, 1212–1218.

53 B. Kaduk, T. Kowalczyk and T. Van Voorhis, *Chem. Rev.*, 2011, **112**, 321–370.

54 J. Hoche, A. Schulz, L. M. Dietrich, A. Humeniuk, M. Stolte, D. Schmidt, T. Brixner, F. Würthner and R. Mitric, *Chem. Sci.*, 2019, **10**, 11013–11022.

55 H.-S. Ren, M.-J. Ming, J.-Y. Ma and X.-Y. Li, *J. Phys. Chem. A*, 2013, **117**, 8017–8025.

56 J. E. Norton and J.-L. Brédas, *J. Am. Chem. Soc.*, 2008, **130**, 12377–12384.

57 D. P. McMahon and A. Troisi, *J. Phys. Chem. Lett.*, 2010, **1**, 941–946.

58 T. Xu, W. Wang and S. Yin, *J. Phys. Chem. A*, 2018, **122**, 8957–8964.

59 C. Poelking, E. Cho, A. Malafeev, V. Ivanov, K. Kremer, C. Risko, J.-L. Brédas and D. Andrienko, *J. Phys. Chem. C*, 2013, **117**, 1633–1640.

60 K.-H. Lin, A. Prlj, L. Yao, N. Drigo, H.-H. Cho, M.-K. Nazeeruddin, K. Sivula and C. Corminboeuf, *Chem. Mater.*, 2019, **31**, 6605–6614.

61 S. Canola and F. Negri, *J. Phys. Chem. C*, 2015, **119**, 11499–11505.

62 S. Di Motta, M. Siracusa and F. Negri, *J. Phys. Chem. C*, 2011, **115**, 20754–20764.

63 S. M. Gali, M. Matta, B. H. Lessard, F. Castet and L. Muccioli, *J. Phys. Chem. C*, 2018, **122**, 2554–2563.

64 W. F. Pasveer, J. Cottaar, C. Tanase, R. Coehoorn, P. A. Bobbert, P. W. M. Blom, D. M. de Leeuw and M. A. J. Michels, *Phys. Rev. Lett.*, 2005, **94**, 206601.

65 S. Giannini, A. Carof, M. Ellis, H. Yang, O. G. Ziogos, S. Ghosh and J. Blumberger, *Nat. Commun.*, 2019, **10**, 3843.

66 T. Nematiaram and A. Troisi, *Mater. Horiz.*, 2020, **7**, 2922–2928.

67 T. F. Harrelson, V. Dantanarayana, X. Xie, C. Koshnick, D. Nai, R. Fair, S. A. Nuñez, A. K. Thomas, T. L. Murrey, M. A. Hickner, J. K. Grey, J. E. Anthony, E. D. Gomez, A. Troisi, R. Faller and A. J. Moulé, *Mater. Horiz.*, 2019, **6**, 182–191.

68 N. G. Martinelli, Y. Olivier, S. Athanasopoulos, M.-C. Ruiz Delgado, K. R. Pigg, D. A. da Silva Filho, R. S. Sánchez-Carrera, E. Venuti, R. G. Della Valle, J.-L. Brédas and D. Beljonne, *ChemPhysChem*, 2009, **10**, 2265–2273.

69 T. He, Y. Wu, G. D'Avino, E. Schmidt, M. Stolte, J. Cornil, D. Beljonne, P. P. Ruden, F. Würthner and C. D. Frisbie, *Nat. Commun.*, 2018, **9**, 2141.

70 V. Coropceanu, R. S. Sánchez-Carrera, P. Paramonov, G. M. Day and J.-L. Brédas, *J. Phys. Chem. C*, 2009, **113**, 4679–4686.

71 P. Gosar and I. Vilfan, *Mol. Phys.*, 1970, **18**, 49–61.

72 X. Xie, A. Santana-Bonilla and A. Troisi, *J. Chem. Theory Comput.*, 2018, **14**, 3752–3762.

**10864** | *J. Mater. Chem. C*, 2021, **9**, 10851–10864

This journal is © The Royal Society of Chemistry 2021